nature communications

Article

https://doi.org/10.1038/s41467-026-77245-1

Iontrovoltaic effect based on triboelectrically induced ion polarization at semiconductor-liquid interfaces

Received: 22 February 2026

Accepted: 18 August 2026

Published online: 26 August 2026

Check for updates

Xiang Li[1], Yu Wei[1], Yaowen Ouyang[1], Zhong Lin Wang[1], Yuying Cao[2] ✉ & Di Wei[1,3] ✉

Controlling interfacial energy levels at semiconductor-liquid interfaces is critical yet challenging because charge separation is dictated by coupled semiconductor band bending and electrical double layers. Existing chemical and electrical regulation strategies inevitably require invasive treatments or external energy input. Here, we propose an iontrovoltaic mechanism, in which asymmetric electrical double layers establish ionic concentration gradients driving ionic directional migration. Triboelectrically induced ionic polarization simultaneously modulates electrical double layers and semiconductor band bending, enhancing the coupled electrical double layer-space charge region field to promote photocarrier separation. Coupled interfacial oxidation and ionic migration enable efficient ionic-electronic transport in iontrovoltaic nanogenerators. Local pH mapping, Kelvin probe measurements, and Mott-Schottky analysis confirm coupled ionic redistribution and band modulation. Integrating alkaline oxidation and infrared photothermal activation yields redox-coupled iontrovoltaic nanogenerators with a peak power density of 541 W m^{-2}, exceeding representative triboelectric, tribovoltaic, and triboiontronic systems. By coupling dynamic electrical double layer programming with semiconductor band modulation, iontrovoltaic effect establishes interfacial electrostatics as an active driver of energy conversion and ionic transport, opening opportunities for autonomous, low-power ionic-electronic systems.

Energy conversion and utilization represent one of the most fundamental challenges facing humanity[1–4]. Across technologies ranging from energy harvesting to catalysis, the efficiency with which energy can be converted, stored, and utilized is ultimately governed by the regulation of interfacial energy levels that control charge separation and transport[5–7]. In particular, semiconductor-liquid interfaces underpin a broad class of solar-to-electrical and solar-to-chemical energy conversion systems, including photocatalysis[8,9], photoelectrochemistry[10,11], and emerging optoelectronic-ionic hybrid devices[12–14]. Despite decades of progress in materials design, the efficient separation and directional transport of charge carriers across these interfaces remains a central bottleneck limiting performance and scalability.

A wide range of strategies has been developed to promote interfacial charge separation. Band-structure engineering through compositional tuning[15–17], heterojunction formation[18,19], and quantum confinement has enabled precise control over electronic energy levels[20,21], exemplified by quantum-dot technologies whose impact was recognized by the Nobel Prize[22,23]. However, such approaches are intrinsically constrained by material complexity, elemental toxicity,

[1]Beijing Key Laboratory of High-Entropy Energy Materials and Devices, Beijing Institute of Nanoenergy and Nanosystems, Chinese Academy of Sciences, Beijing, P. R. China. [2]School of Mechanical Engineering, Yanshan University, Qinhuangdao, P. R. China. [3]Centre for Photonic Devices and Sensors, University of Cambridge, 9 JJ Thomson Avenue, Cambridge, UK. ✉e-mail: yuyingcao@ysu.edu.cn; weidi@binn.cas.cn

and resource scarcity, limiting their long-term sustainability and broad deployment. Surface modification and defect engineering can enhance local electric fields, yet often introduce recombination centers and suffer from limited stability[24,25]. External electrical bias provides a more direct driving force for charge separation, but at the cost of additional energy input, device complexity, and departure from intrinsic energy conversion processes[26,27]. More recently, electrolyte and solvent engineering have been explored to manipulate the electrical double layer (EDL) and interfacial energetics[28–31], although these methods are generally highly system-specific, chemically invasive, and fundamentally limited by ionic screening.

These challenges are particularly acute at semiconductor-liquid interfaces. Unlike solid-solid semiconductor junctions, where carrier dynamics are largely dictated by static band alignment, semiconductor-liquid interfaces are governed by a multiscale and dynamically evolving electrostatic environment[32,33]. Charge separation is controlled by the coupled interplay among semiconductor band bending[34], surface states[35], solvent reorganization[36], and the EDL[37,38], with ionic distributions that continuously evolve in space and time. This coupling gives rise to strong field screening and intrinsically nonequilibrium charge-transfer processes that critically limit carrier lifetimes, transport pathways, and interfacial reactivity. Consequently, interfacial charge separation is not solely an intrinsic property of the semiconductor, but an emergent phenomenon defined by the spatiotemporal distribution of electric fields across the coupled semiconductor-EDL system. Despite sustained advances, existing strategies remain fundamentally restricted by electrostatic screening, reliance on chemical or structural modification, or the need for external power sources.

Here, we proposed a fundamentally different physical approach to interfacial energy-level regulation based on triboelectrically induced ion polarization. Arising from contact electrification between dissimilar materials[39–41], triboelectric polarization is a ubiquitous interfacial phenomenon that generates surface charge accumulation and macroscopic electrostatic fields without external bias or chemical modification[42,43]. This polarization was demonstrated to serve as a noncontact and dynamically tunable means to regulate interfacial electrostatics at semiconductor-liquid interfaces. Specifically, the externally generated polarization field could simultaneously redistribute ionic species within the EDL and modulate semiconductor band bending, thereby enhancing the built-in electric field in the coupling region between the EDL and the space charge region (SCR) and suppressing interfacial recombination. Therefore, it could overcome longstanding limitations imposed by electrostatic screening and nonequilibrium charge dynamics at solid-liquid interfaces. Crucially, unlike conventional strategies based on static material design, this approach could enable active and reversible control of interfacial energy landscapes without altering material composition or introducing additional energy input. By decoupling interfacial regulation from intrinsic material properties, it provided a general and non-invasive route for dynamically tuning charge separation and transport at solid-liquid interfaces.

Building on this capability, we introduce the term iontrovoltaic effect to describe electricity generation driven by directional ionic transport arising from dynamically programmed asymmetric EDLs at semiconductor-liquid interfaces. In this iontrovoltaic paradigm, asymmetric EDLs establish ionic concentration gradients that, when coupled with triboelectric, optical (ultraviolet, UV), and thermal (infrared, IR) stimuli, enable programmable charge transport. These asymmetric EDL states can be temporally encoded, allowing nominally identical interfaces to evolve into dynamically reconfigurable ionic concentration gradients that dictate transport directionality. Triboelectrically induced ion polarization simultaneously modulates ionic redistribution within the EDL and semiconductor band bending, thereby amplifying the built-in electric field in the SCR-EDL coupling region and promoting efficient photocarrier separation. The resulting hole-driven interfacial oxidation generates additional ionic species, reinforcing EDL asymmetry and sustaining directional transport through a positive feedback loop. This coupled regulation is supported by complementary interfacial probes: local pH mapping reveals polarization-driven ionic redistribution, while Kelvin probe force microscopy (KPFM) and Mott-Schottky analysis confirm reversible modulation of the semiconductor work function and band bending. Together, these effects underpin the operation of the iontrovoltaic nanogenerator (IVNG), where ionic migration efficiency is enhanced by ~2.9 times compared to diffusion driven solely by asymmetric EDLs. Further tuning of the solid-phase work-function contrast and liquid-phase ionic composition introduces interfacial redox processes, leading to the redox-coupled iontrovoltaic nanogenerator (RC-IVNG). This provides additional degrees of freedom for regulating EDL charge density, ionic mobility, and reaction pathways. Through these synergistic mechanisms, the RC-IVNG achieves a peak power (P_R) density of 541 W m^{-2}, surpassing triboelectric, tribovoltaic, and triboiontronic systems under comparable conditions. More importantly, this cooperative ionic-electronic coupling unifies energy conversion, matter transport, and information processing within a single interfacial framework. The optically programmable EDL landscape further enables light-driven iontronic logic gating, allowing dynamic reconfiguration of ionic transport pathways and Boolean operations. By demonstrating that EDLs can actively promote, rather than merely screen, charge separation, the iontrovoltaic effect revises the conventional view of interfacial electrostatics. This work establishes triboelectrically induced ion polarization as a remote, dynamic, and chemical-free strategy for modulating interfacial energy landscapes, providing a foundation for programmable ionic-electronic systems.

Results

Mechanism of the iontrovoltaic effect inspired by the neural synapse

Biological neural systems achieve fast, robust, and low-power information processing by regulating ionic fluxes across nanoscale interfaces. Despite operating at only ~20 W, the human brain sustains complex computation through hierarchical ionic signaling, in which long-range propagation along axons and localized synaptic transmission are both governed by interfacial ionic transport (Fig. 1a). In this manner, matter transport, energy flow, and information processing are intrinsically coupled through ionic dynamics. Inspired by this paradigm, an iontrovoltaic framework was proposed in which nominally identical semiconductor-liquid interfaces evolve into asymmetric electrostatic states through temporal encoding, thereby establishing an artificial ionic concentration gradient. When coupled with external triboelectric fields, optical excitation (UV illumination), and thermal stimuli (IR irradiation), this gradient enables programmable ionic transport. Notably, this process exhibits a functional analogy to synaptic signaling: optical excitation acts as a stimulus that triggers interfacial charge separation, analogous to action potential activation, while subsequent interfacial reactions generate and release mobile ionic species that propagate across the interface, reminiscent of neurotransmitter-mediated signal transmission. Based on this principle, an IVNG was developed (Fig. 1b), which enables coupled energy conversion and light-modulated ionic signal processing, providing a platform for integrated iontronic functionalities.

The iontrovoltaic mechanism is schematically illustrated in Fig. 1c. When a water droplet contacts the bottom p-Si/Au electrode, the Fermi level mismatch at the semiconductor-liquid interface induces charge redistribution, resulting in electron transfer from water into the semiconductor and the formation of a micrometer-scale negatively charged SCR [Fig. 1c(i)]. Simultaneously, partial electron transfer and interfacial hydrolysis generate surface-bound anionic species, establishing a negatively charged inner Helmholtz layer. Electrostatic

https://doi.org/10.1038/s41467-026-77245-1

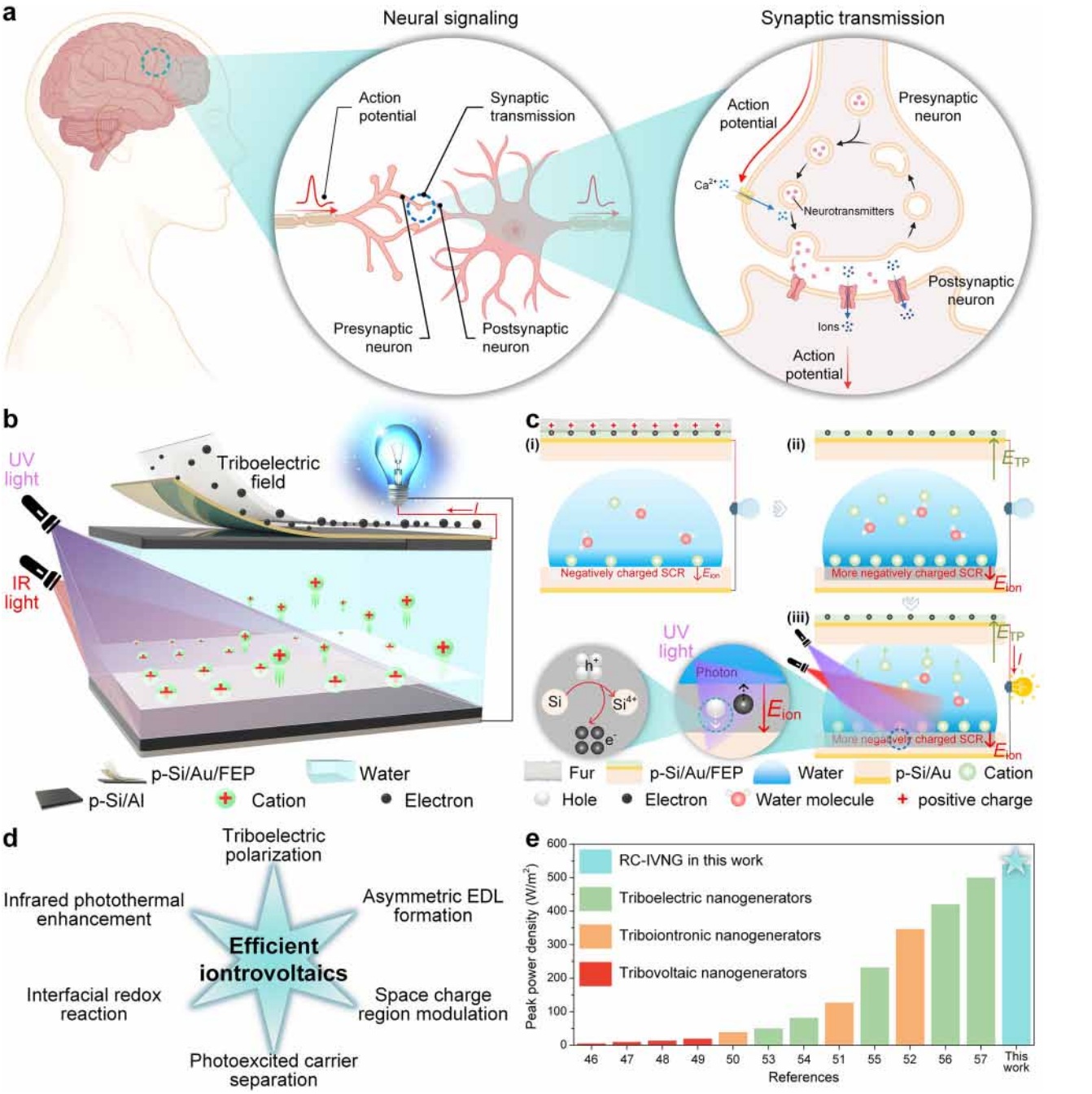


Fig. 1 | Neural inspiration and interfacial mechanism of the iontrovoltaic effect. **a** Multilevel organization of neural information processing, culminating in ion-mediated synaptic transmission. The blue dotted line represents synaptic transmission pathways, involving neurotransmitter release and reception at the synaptic interface. Created in BioRender. Li, X. (2026) https://BioRender.com/dl2vb37. **b** Schematic illustration of the iontrovoltaic nanogenerator (IVNG), which biomimetically replicates synaptic ionic transport regulated by charge dynamics through triboelectrically induced ion polarization at semiconductor-liquid interfaces. **c** Schematic illustration of the iontrovoltaic mechanism in the IVNG. Interfacial electrostatics regulated by triboelectrically induced ionic polarization and UV/IR stimuli generate asymmetric electrical double layers and a built-in field, driving directional ion transport. The blue dotted line dashed lines indicate photo-generated charge carrier separation within the semiconductor SCR. **d** Multiphysics coupling in the iontrovoltaic effect, integrating triboelectric polarization, asymmetric electrical double layers (EDLs) formation, space charge region (SCR) modulation, photoinduced carrier separation, interfacial redox reaction, and IR photothermal enhancement. **e** Output power comparison showing the redox-coupled iontrovoltaic nanogenerator (RC-IVNG) surpassed typical triboelectric, tribovoltaic, and triboiontronic nanogenerators.

interactions then drive cation accumulation to form the outer Helmholtz layer and diffuse layer, completing the nanometer-scale EDL structure[44,45] (Supplementary Fig. 1). The EDL develops a net positive countercharge that compensates the negatively charged SCR, maintaining interfacial electroneutrality. The coupled SCR-EDL configuration establishes a built-in electric field E_{ion}, which governs subsequent charge separation and ionic transport. To actively regulate E_{ion}, triboelectric polarization is introduced by laminating an electronegative fluorinated ethylene propylene (FEP) film onto the top electrode and rubbing it with electropositive fur. Upon separation, trapped charges on FEP generate an external electrostatic field E_{TP} [Fig. 1c(ii)], which remotely enhances electron transfer into p-Si and strengthens band

bending, while simultaneously driving ionic redistribution in the EDL, characterized by anion enrichment near the surface and cation accumulation in the adjacent liquid (Supplementary Fig. 2). This coupled modulation increases the densities of oppositely charged species in the SCR and EDL, reinforcing interfacial charge compensation and significantly enhancing E_{ion}. When the identical top p-Si/Au electrode contacts the droplet, a second EDL forms instantaneously. The contrast between the strongly polarized bottom EDL and the relatively weakly polarized top EDL establishes an ionic concentration gradient that drives directional cation migration across the liquid layer [Fig. 1c(iii)]. Photoexcitation further amplifies this coupling: under UV illumination, photogenerated carriers are separated by the enhanced E_{ion}, enabling hole-driven Si oxidation and generating additional ionic species that reinforce EDL asymmetry. IR irradiation increases ionic mobility via photothermal activation, further enhancing ion flux. Through the synergistic coupling of triboelectric polarization, asymmetric EDLs formation, SCR modulation, photoinduced carrier separation, interfacial redox reaction, and IR photothermal enhancement, the IVNG constructs a dynamically reconfigurable ionic energy landscape that enables robust and directional ion transport (Fig. 1d).

Building on this framework, introducing solid-phase work-function asymmetry and tuning the liquid ionic composition enables additional semiconductor oxidation, giving rise to an RC-IVNG. This strategy provides additional degrees of freedom for controlling EDL charge density, ionic mobility, and interfacial reaction pathways. As a result, the RC-IVNG achieves a P_R density of 541 W m^{-2} (Fig. 1e), substantially exceeding that of typical tribovoltaic nanogenerators[46–49], triboiontronic nanogenerators[50–52], and triboelectric nanogenerators[53–57]. Tribovoltaic nanogenerators rely on friction-induced carrier excitation at semiconductor interfaces (Supplementary Fig. 3), triboiontronic nanogenerators are governed by EDL-driven ionic migration (Supplementary Fig. 4), and triboelectric nanogenerators operate via contact electrification and electrostatic induction (Supplementary Fig. 5). These mechanisms are generally limited by insufficient interfacial field strength or the lack of coupled ionic-electronic regulation. In contrast, the iontrovoltaic effect integrates electrostatic modulation, photocarrier dynamics, and interfacial physicochemical processes within a unified framework, enabling actively coupled ionic transport. Notably, although some reported systems exhibit higher apparent power densities, these typically rely on micrometer-scale contact areas[58] or complex circuit designs[59]. By comparison, the RC-IVNG operates in a conventional contact-separation mode with a macroscopic contact area (1 cm^2) and without circuit optimization, enabling a direct and practically relevant performance evaluation. These results establish the iontrovoltaic effect as a paradigm for higher-efficiency ionic transport and solid-liquid energy conversion.

Directional ionic migration induced by temporally programmed asymmetric EDLs at semiconductor-liquid interfaces

To determine whether nominally identical semiconductor-liquid interfaces can be temporally programmed to generate asymmetric EDLs capable of directing ionic migration, a sequential wetting protocol was implemented. The Fermi level of p-Si lies below that of water (Fig. 2a). Upon contact of the bottom p-Si/Au electrode with a water droplet for 10 s, Fermi level mismatch induces band bending and charge redistribution (Fig. 2b), resulting in electron transfer from water into the semiconductor and the formation of a negatively charged SCR (Fig. 2c). Concurrently, interfacial electron transfer and hydrolysis generate surface-bound anionic species, establishing the inner Helmholtz layer. Together with cation accumulation and diffuse-layer formation, a stable bottom EDL is formed, which develops a net positive countercharge compensating the negatively charged SCR and maintaining interfacial electroneutrality (Fig. 2d). Subsequently, an identical top p-Si/Au electrode is introduced and electrically connected via Au layers to serve as charge collection electrodes (Fig. 2e). Upon contact, a second EDL forms at the top interface. Due to distinct formation histories, the two interfaces exhibit different interfacial charge densities, giving rise to asymmetric EDLs (Fig. 2f). The resulting ionic concentration gradient drives directional cation migration across the droplet, producing an open-circuit voltage (V_{OC}) of 0.1 V, a short-circuit current (I_{SC}) of 2.5 μA, and a transferred charge (Q_{SC}) of 0.13 μC (Fig. 2g, h and Supplementary Fig. 6). Reversing the wetting sequence inverts the EDL asymmetry and reverses the output polarity (V_{OC} of − 0.07 V, I_{SC} of − 1.4 μA, Q_{SC} of − 0.072 μC), while equal wetting durations suppress output generation. Similar behavior is observed for n-Si/Au electrodes (Supplementary Figs. 7–9), which exhibit identical wetting-order-dependent polarity, confirming that temporally programmed asymmetric EDLs formation is a universal mechanism independent of semiconductor doping. Collectively, these results demonstrate that ionic migration is governed by the gradient of asymmetric EDLs, while its magnitude is determined by the degree of EDL asymmetry.

Synergistic enhancement of directional ionic transport through triboelectrically induced ion polarization, SCR modulation, and photoexcitation

The directional migration driven by ionic concentration gradients between asymmetric EDLs constitutes the basis of the iontrovoltaic effect. For a mobile ionic species with valence z, the ion gradient potential μ is expressed as

$$\mu = k_B T \ln c + ze\phi, \tag{1}$$

where c is the local ionic concentration, ϕ is the electrostatic potential, k_B is the Boltzmann constant, T is the absolute temperature, and e is the elementary charge. Spatial gradients in μ drive ionic migration across the liquid layer, giving rise to an ionic flux

$$J_{ion} \approx -\frac{D}{L}\left[\Delta c + \frac{ze\bar{c}}{k_B T}\Delta\phi\right] \tag{2}$$

where D is the ionic diffusion coefficient, L is the effective liquid thickness, Δc and $\Delta\phi$ denote the concentration and electrostatic potential differences between the bottom and top EDLs, respectively, and $\bar{c}$ is the average ionic concentration. It indicates that directional ionic transport is jointly governed by chemical asymmetry (Δc) and electrical asymmetry ($\Delta\phi$) between the two interfaces. Upon UV illumination, electron-hole pairs are generated within the semiconductor. The built-in electric field E_{ion} established in the coupled SCR-EDL region drives electrons and holes in opposite directions, initiating charge separation. However, the effectiveness of this interfacial field is fundamentally constrained by both the EDL and SCR. On the liquid side, the EDL thickness is governed by the Debye length (λ_D)

$$\lambda_D = \sqrt{\frac{\varepsilon_r \varepsilon_0 k_B T}{e^2 \Sigma_i n_i z_i^2}}, \tag{3}$$

where ε_r and ε_0 are the relative permittivity of the medium and the vacuum permittivity, respectively, n_i and z_i denote the number density and valence of the i-th ionic species. Increasing ionic concentration reduces λ_D, resulting in a more compact EDL and a locally enhanced interfacial field. However, excessive ionic strength leads to pronounced electrostatic screening, which attenuates the effective field penetration and hinders directional charge separation and transport. On the semiconductor side, the SCR width is determined by the doping concentration. Under the depletion approximation, the SCR width W scales as

$$W = \sqrt{\frac{2\varepsilon_s \Delta\psi_{SCR}}{qN}} \tag{4}$$

https://doi.org/10.1038/s41467-026-77245-1

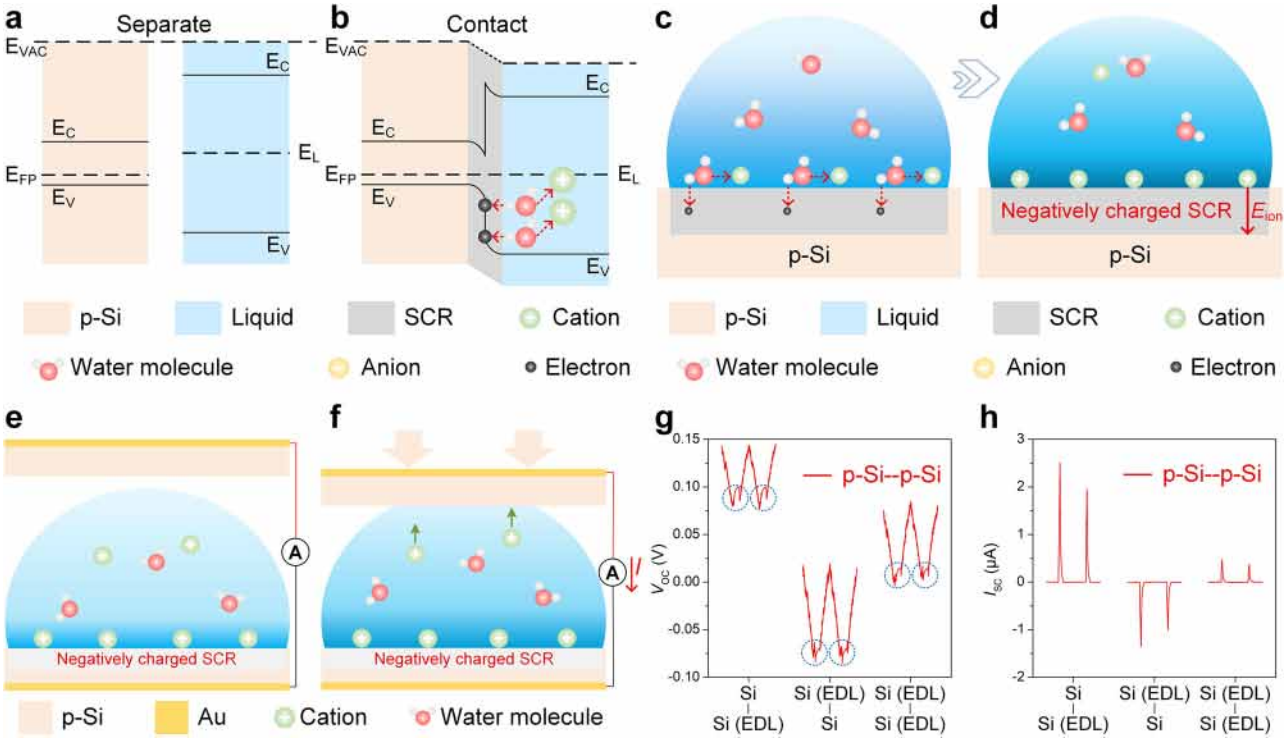


Fig. 2 | Directional ionic migration governed by temporally programmed asymmetric EDLs at semiconductor-water interfaces. a The Fermi level of p-Si lies below that of water. **b** Upon contact between a water droplet and the p-Si/Au electrode, the Fermi level mismatch at the semiconductor-liquid interface induces band bending and charge redistribution. E_{VAC}, vacuum energy level; E_C, conduction band minimum; E_V, valence band maximum; E_{FP}, Fermi level of p-Si; E_L, electron electrochemical potential (redox Fermi level) of the liquid. **c** Electron transfer from water into the semiconductor leads to the formation of a negatively charged SCR. **d** Coupled SCR-EDL structure at the p-Si-water interface, consisting of a negatively charged SCR and a positively charged EDL. SCR, space charge region; E_{ion}, built-in electric field established by the coupled SCR-EDL structure. **e**, **f** Sequential wetting of nominally identical semiconductor-liquid interfaces generates asymmetric EDLs capable of directing ionic migration. The arrows indicate cation migration direction. **g**, **h** V_{OC} and I_{SC} induced by asymmetric EDLs in the p-Si system. The blue dashed lines represent the V_{OC}.

where ε_s is the semiconductor permittivity, $\Delta\psi_{SCR}$ is the potential drop across the SCR, q is the elementary charge, and N is the doping concentration. Increasing doping reduces the SCR width and enhances the local electric field. Nevertheless, excessive doping narrows the SCR, limits the spatial region for charge separation, and accelerates carrier recombination. In addition, it may introduce defect states and reduce carrier mobility, further suppressing charge transport. These competing constraints highlight a fundamental challenge: conventional strategies based on ionic strength or doping can enhance local electric fields, but often at the expense of either spatial extension or transport efficiency. Therefore, a non-invasive and dynamically tunable approach is required to simultaneously regulate EDL ionic distribution and semiconductor band bending. In this context, triboelectric polarization provides an effective strategy to overcome these limitations by dynamically modulating both the EDL and SCR, enabling enhanced interfacial electric fields and efficient charge separation beyond conventional approaches. When the electronegative FEP layer atop the p-Si/Au electrode is rubbed with electropositive fur, excess electrons are transferred to and trapped on the FEP surface, generating an external electrostatic field E_{TP} (Fig. 3a). This field can be equivalently described as a triboelectrically imposed interfacial potential bias $\Delta\psi_{TP}$, which predominantly couples to the bottom semiconductor-liquid interface. Within a first-order electrostatic framework, this imposed potential is partitioned between the semiconductor SCR and the liquid-side EDL according to their series capacitances,

$$\Delta\psi_{TP} \approx \Delta\psi_{SCR} + \Delta\psi_{EDL}, \tag{5}$$

with the partition governed by the series capacitances C_{SCR} and C_{EDL}. As a result, the interfacial potential at the bottom interface is elevated to

$$\psi_b = \psi_b^0 + \Delta\psi_{TP}, \tag{6}$$

where ψ_b^0 is the intrinsic interfacial potential established upon semiconductor-liquid contact. Within the diffuse layer, the ionic concentration follows a Boltzmann distribution,

$$c(x) = c_0 \exp\left[-\frac{ze\psi_b}{k_B T}\right], \tag{7}$$

indicating that an increase in ψ_b exponentially enriches counter-ions and depletes co-ions near the interface.

Consequently, both the Stern and diffuse layers of the bottom EDL become more densely populated, leading to an enlarged ionic concentration difference Δc. Meanwhile, the redistribution and amplification of the interfacial potential enhance semiconductor band bending and suppress interfacial recombination of photogenerated carriers. The resulting cooperative coupling between SCR and EDL fields strengthens the built-in electric field E_{ion} in the SCR-EDL region, promoting efficient charge separation and further increasing the potential difference $\Delta\phi$ between the two EDLs. Through this coupled amplification of electrostatic and ionic asymmetry, the ion gradient potential across the liquid layer is significantly enhanced. The resulting

https://doi.org/10.1038/s41467-026-77245-1

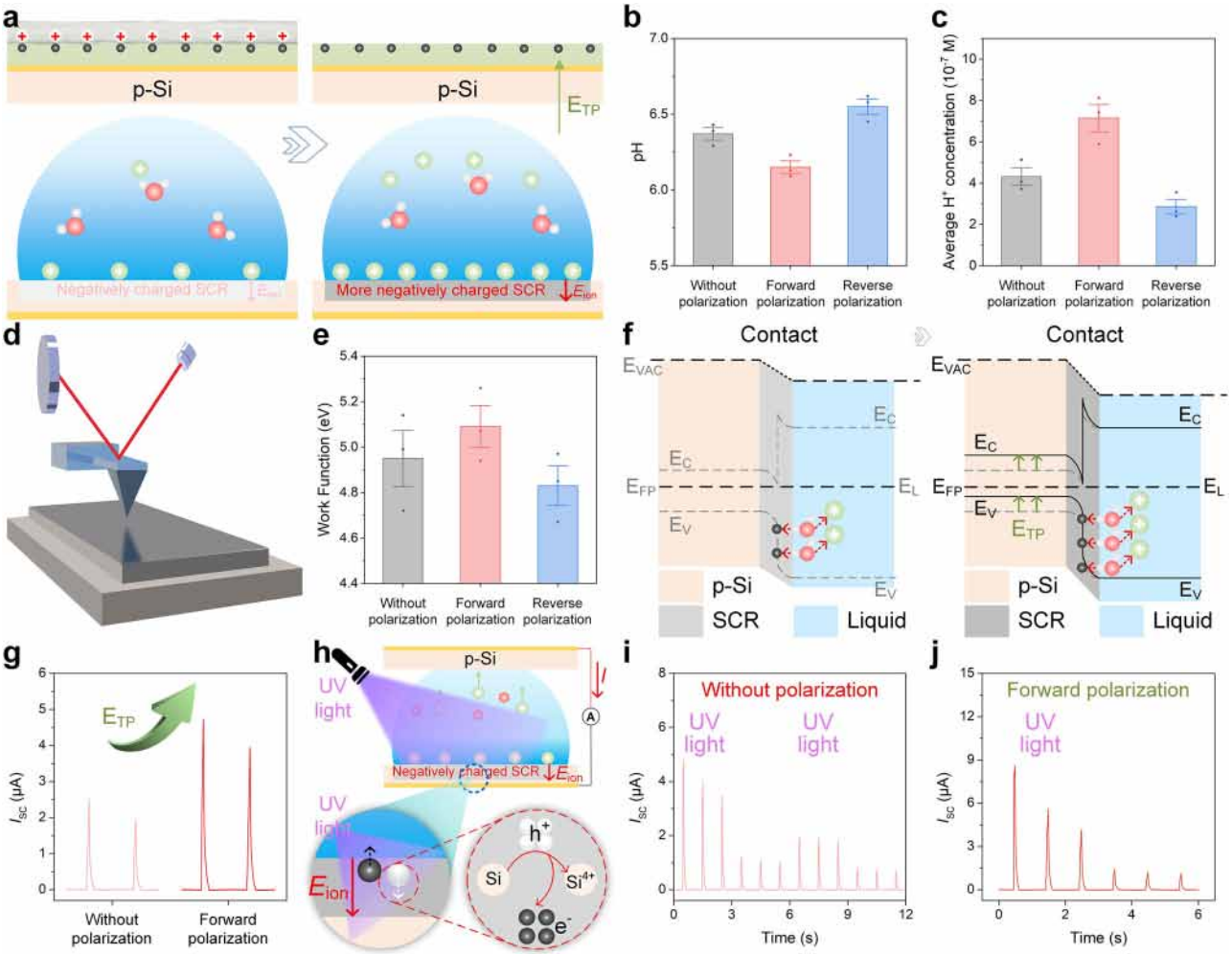


Fig. 3 | Triboelectrically induced ion polarization enhances interfacial electrostatics and promotes carrier separation, enabling an efficient IVNG. **a** Schematic illustration of long-range modulation of EDL ionic distribution and semiconductor band bending by triboelectric polarization. **b** Local pH maps near the p-Si-water interface under different polarization conditions. Error bars represent the standard deviation based on three replicate data. Source data are provided as a Source Data file. **c** Corresponding H^+ concentration profiles extracted from the pH measurements. Error bars represent the standard deviation based on three replicate data. Source data are provided as a Source Data file. **d** Surface work function measured by the KPFM under different polarization states. **e** Extracted work function of p-Si under different polarization conditions. Error bars represent the standard deviation based on three replicate data. Source data are provided as a Source Data file. **f** Polarization-induced increase in work function enhances the Fermi level difference between p-Si and water, strengthening interfacial band bending. **g** Enhanced directional ion migration in asymmetric EDLs under triboelectric polarization, reflected by increased I_{SC}. **h** Photoinduced carrier separation and hole-driven interfacial oxidation at the p-Si-water interface. The blue dotted line dashed lines indicate photogenerated charge carrier separation within the semiconductor SCR. **i** Photoexcitation-enhanced ionic output via hole-mediated interfacial reactions and EDL ion enrichment. **j** Synergistic amplification of ionic transport under combined triboelectric polarization and photoexcitation.

ionic flux and corresponding I_{SC} are therefore increased according to

$$I_{SC} = AzeJ_{ion}, \tag{8}$$

where A is the effective interfacial area. These results demonstrate that triboelectrically induced ion polarization, in synergy with photoexcitation, dynamically amplifies interfacial electrostatics, suppresses carrier recombination, and converts efficient photogenerated charge separation into a macroscopic, directional ionic current.

Guided by the above theoretical framework, whether triboelectric polarization can actively modulate ionic redistribution within the EDL was experimentally investigated. Three representative interfacial configurations were examined: (i) a pristine p-Si-water interface without polarization, (ii) forward polarization induced by positioning a negatively charged FEP film above the liquid, and (iii) reverse polarization generated by placing a positively charged fur layer above the liquid. The polarization-induced modulation of ionic populations was directly probed through local pH measurements near the semiconductor-water interface (Supplementary Fig. 10). In the absence of external polarization, the average pH near the p-Si-water interface was ~6.37 (Fig. 3b), corresponding to an H^+ concentration of ~4.3×10^{-7} M (Fig. 3c). Under forward polarization, the pH decreased to ~6.15, generating an increased H^+ concentration of ~7.1×10^{-7} M, consistent with electrostatic enrichment of counter-ions. In contrast, reverse polarization increased the pH to ~6.55, reducing the H^+ concentration to ~2.8×10^{-7} M. To exclude the potential influence of interfacial electrochemical reactions under strong fields and illumination, the semiconductor substrate was replaced with an inert dielectric layer (Polytetrafluoroethylene, PTFE), and the measurements were repeated under identical conditions (Supplementary Fig. 11). The observed pH variations and corresponding H^+ concentrations exhibited the same systematic trends and full reversibility upon switching the polarization direction, consistent with those measured at the p-Si-water interface (Supplementary Figs. 12, 13).

Notably, due to the larger electronegativity difference between PTFE and water, which leads to a more compact EDL, the pH and ionic concentration changes were even more pronounced. These systematic and reversible pH responses provide direct experimental evidence that triboelectrically induced ion polarization dynamically reshapes the ionic distribution within the EDL. To further examine whether triboelectric polarization can modulate semiconductor energy levels, the work function of p-Si was first measured by KPFM under dry conditions (Fig. 3d). Under forward polarization, introduced by placing a positively charged nylon layer near the backside of the p-Si/Au electrode, the average work function increases from 4.95 to 5.09 eV (Fig. 3e). Conversely, under reverse polarization, induced by a negatively charged PTFE layer, it decreases to ~ 4.83 eV. These results indicate that triboelectric polarization induces reversible surface potential variation on the semiconductor. To validate whether such modulation persists under operando semiconductor-liquid conditions, in situ electrochemical measurements based on Mott-Schottky analysis were performed to directly probe band bending at the p-Si-water interface under different triboelectric polarization states (Supplementary Fig. 14). Under forward polarization, the flat-band potential shifts positively, indicating enhanced band bending and increased SCR charge density (Fig. 3f and Supplementary Fig. 15). In contrast, reverse polarization induces a negative shift of the flat-band potential, consistent with reduced band bending and a weakened SCR field (Supplementary Figs. 16, 17). Importantly, although KPFM and Mott-Schottky analysis probe different environments, the consistent trend in work function and flat-band potential shifts confirms that triboelectrically induced polarization can reversibly modulate semiconductor band bending. Combined with the concurrent redistribution of ionic species within the EDL, this modulation enhances the built-in electric field E_{ion} in the SCR-EDL coupling region.

The influence of triboelectric polarization on the efficiency of directional ionic migration in asymmetric EDLs at two p-Si-water interfaces was quantitatively analyzed (Supplementary Fig. 18). Under dark conditions, forward polarization leads to pronounced enhancements in output signals relative to ionic migration driven solely by asymmetric EDLs, with I_{SC} increasing from ~ 2.5;μA to ~ 4.7 μA, V_{OC} from ~ 0.1 V to ~ 0.15 V, and Q_{SC} from ~ 0.13 μC to ~ 0.23 μC (Fig. 3g and Supplementary Figs. 19, 20). Therefore, triboelectric polarization provides an effective and quantitative strategy for enhancing directional ion transport in asymmetric EDL systems. To further elucidate the coupling between the photovoltaic process and asymmetric EDLs, photoexcitation experiments were conducted in the IVNG. In the absence of triboelectric polarization, UV illumination of the bottom p-Si in the asymmetric EDLs system could generate an effective electrical output (Fig. 3h). Compared with the I_{SC} of ~ 2.5 μA driven solely by asymmetric EDLs-induced ionic migration, photoexcitation increases I_{SC} to ~ 4.8 μA (Fig. 3i), and Q_{SC} is significantly enhanced from ~ 0.13 μC to ~ 0.29 μC (Supplementary Fig. 21). A slight reduction in V_{OC} to 0.08 V reflects partial consumption of interfacial potential for photocarrier separation (Supplementary Fig. 22). This behavior arises from the built-in electric field E_{ion} within the SCR-EDL coupling region, which drives efficient separation of photogenerated carriers and promotes hole migration toward the semiconductor interface for controlled oxidation reactions, generating H^+ ions. The resulting increase in ionic concentration further reinforces EDL asymmetry and drives effective ionic directional transport. Notably, all photoinduced enhancements vanished immediately after illumination was removed, confirming their origin in reversible interfacial processes rather than permanent chemical modification. When triboelectrically induced ion polarization is combined with UV illumination in the IVNG, a pronounced synergistic enhancement is observed, generating I_{SC} of ~ 8.6 μA, V_{OC} of ~ 0.1 V, and Q_{SC} of ~ 0.51 μC (Fig. 3j and Supplementary Figs. 23, 24). Compared with the Q_{SC} of ~ 0.13 μC driven solely by asymmetric EDLs, the ionic transport efficiency is increased by ~ 2.9 times. This enhancement arises from the coupled effect of triboelectric polarization and photoexcitation. Triboelectrically induced ion polarization simultaneously redistributes ionic species within the EDL and modulates semiconductor band bending, thereby strengthening the built-in electric field E_{ion} in the SCR-EDL coupling region. The enhanced field promotes efficient separation of photogenerated carriers and drives hole-mediated interfacial oxidation, generating additional ionic species that further reinforce EDL asymmetry. This positive feedback leads to amplified directional ionic transport and improved overall output performance. In contrast, in the n-Si-based system, triboelectric polarization enhances ionic transport within asymmetric EDLs (Supplementary Fig. 25), whereas no photovoltaic coupling is observed (Supplementary Fig. 26). This difference originates from the opposite interfacial energetics compared to p-Si. For n-Si, the Fermi level lies higher than that of water (Supplementary Fig. 27). Upon contact, electrons transfer from n-Si to the aqueous phase, leading to the formation of a positively charged SCR in the semiconductor (Supplementary Fig. 28). To compensate this charge, the EDL develops a net negative countercharge near the interface (Supplementary Fig. 29). As a result, the built-in electric field E_{ion} in the SCR-EDL coupling region is oriented opposite to that at the p-Si-water interface. Under illumination, this reversed field drives photogenerated holes away from the semiconductor surface, suppressing interfacial redox reactions and thereby preventing effective photovoltaic-ionic coupling (Supplementary Fig. 30). Notably, surface fluorination of n-Si reverses this behavior. Owing to the stronger electron-withdrawing nature of fluorine, electron transfer from water to the fluorinated n-Si surface is promoted (Supplementary Fig. 31), which reconfigures the interfacial charge distribution and reverses the direction of the built-in field in the SCR-EDL region. Consequently, the field orientation becomes analogous to that of the p-Si system, enabling efficient photocarrier separation, interfacial redox reactions, and the generation of effective electrical output in the form of an IVNG (Supplementary Fig. 32). Collectively, the cooperative action of triboelectrically induced ion polarization and photoexcitation provides a powerful mechanism to dynamically tune SCR band energetics, reinforce EDL charge asymmetry, and amplify directional ionic migration. More generally, the iontrovoltaic effect applies to solid-liquid interfaces that support photogenerated charge separation, where interfacial electrostatics can be effectively coupled with carrier dynamics.

Controlling ionic migration through regulation of solid- and liquid-phase material properties

The iontrovoltaic effect originates from the coupling between semiconductor energetics and EDL ionic organization. To elucidate how solid-state band alignment modulates this coupling, we first examined the work-function contrast between p-Si and its metal current collector (Fig. 4a). When Au, Cu, and Al were used sequentially, the IVNG performance increased monotonically, with I_{SC} rising from 8.6 to 20.0 μA, Q_{SC} from 0.29 to 1.24 μC, and V_{OC} from 0.10 to 0.19 V (Fig. 4b and Supplementary Figs. 33 and 34). This trend arises from metal-semiconductor interfacial energetics: higher-work-function Au extracts electrons from p-Si, generating an opposing interfacial field that suppresses carrier extraction (Fig. 4c), whereas lower-work-function Al injects electrons into p-Si, facilitating carrier collection and enhancing ionic-electronic coupling (Fig. 4d). These results demonstrate that band engineering of the solid-state stack provides a deterministic route to tune iontrovoltaic transduction efficiency. Building on this principle, a work-function asymmetry between the top and bottom electrodes is introduced to further regulate interfacial coupling. Replacing the top p-Si/Au electrode with an Au/FEP composite induces two coupled effects. Firstly, water permeates nanoscale fissures in the sputtered Au layer (Supplementary Fig. 35) and contacts FEP, rapidly establishing a top EDL, while the bottom p-Si interface

https://doi.org/10.1038/s41467-026-77245-1

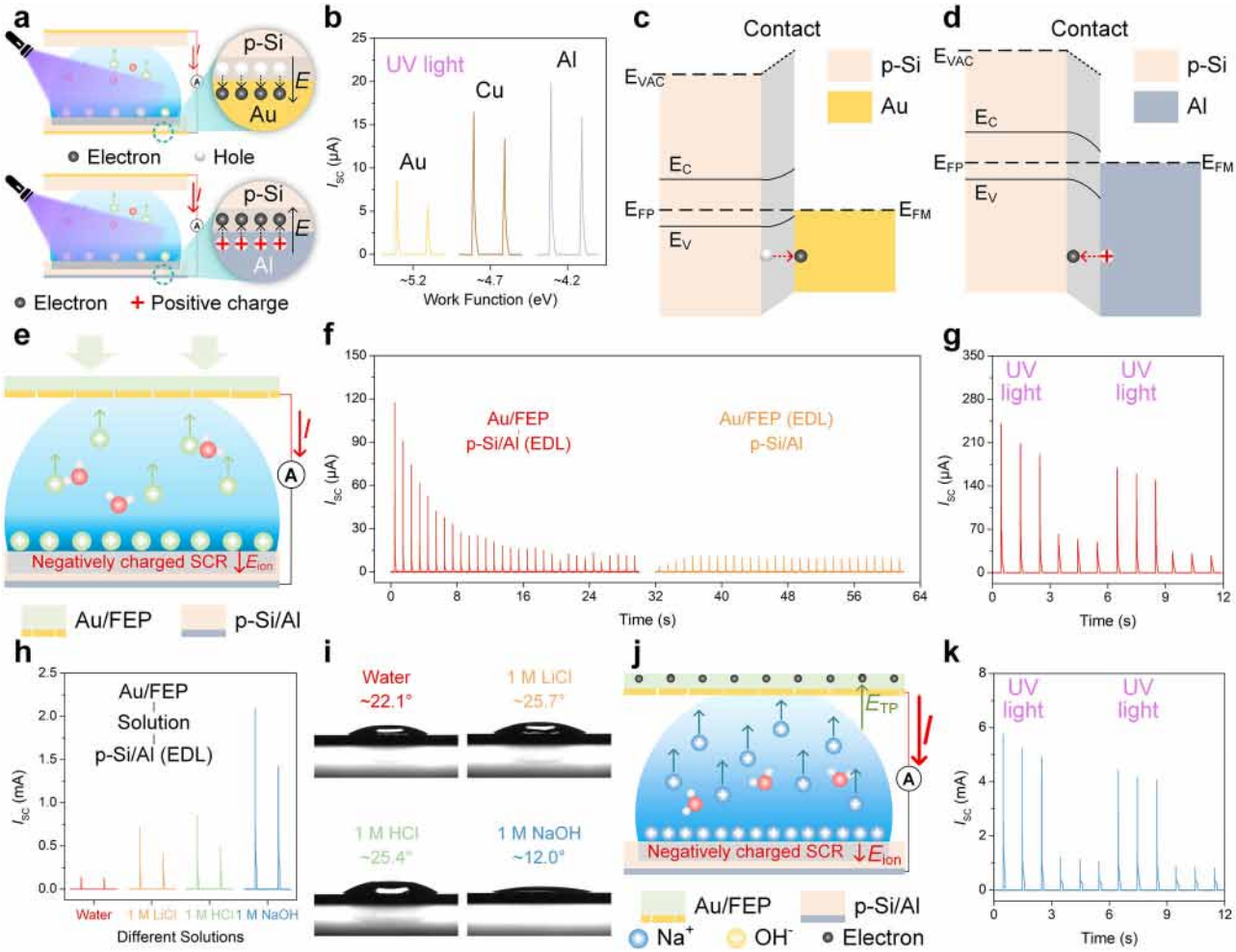


Fig. 4 | Regulation of directional ionic migration through engineered solid- and liquid-phase properties. a Interfacial electric fields at p-Si/metal junctions with different work functions. **b** Output performance of the IVNG using different metal current collectors. **c**, **d** Band alignment at p-Si/Au and p-Si/Al interfaces, illustrating opposite band bending directions and carrier extraction behaviors. **e** Introduction of a work-function asymmetry by replacing the top p-Si/Au electrode with an Au/FEP structure. **f** Transient ionic output arising from the synergistic coupling between asymmetric EDLs and work-function-mediated interfacial redox reactions. **g** Enhancement of I_{SC} under UV illumination due to photoactivated interfacial oxidation at the p-Si-water interface. **h** Effect of electrolyte composition (1 M LiCl, HCl, NaOH) on the output. **i** Contact angles of different electrolytes on p-Si, highlighting enhanced wettability in alkaline conditions. **j** Continuous, non-passivating oxidation of p-Si in NaOH produces sustained ion flux and EDL enrichment. **k** Strongly amplified I_{SC} at the p-Si-NaOH interface under UV illumination in the RC-IVNG, driven by photoactivated interfacial oxidation.

hosts a stabilized EDL (Fig. 4e), forming a strongly asymmetric dual-EDL configuration that drives directional ionic migration. Secondly, the work-function difference between the top Au and bottom p-Si induces interfacial electron redistribution under aqueous conditions, promoting hole-driven oxidation of p-Si and generating additional H^+. This redox process densifies the bottom EDL and couples ionic enrichment with interfacial charge transfer. The cooperative interaction between asymmetric EDLs and redox-driven ionic generation produces a larger transient output ($I_{SC} \approx 117.5$ μA; Fig. 4f), which decays to a stable ~10 μA as the EDL asymmetry relaxes, leaving a redox-dominated steady state. Reversing the wetting sequence inverts the EDL-driven ionic flux, leading to partial cancellation with the redox-driven current and confirming their constructive coupling origin. Finally, incorporating triboelectrically induced ion polarization and photoexcitation further amplifies this mechanism, thereby establishing the RC-IVNG. Under combined forward triboelectric polarization and UV illumination, the RC-IVNG delivers I_{SC} of 241 μA, Q_{SC} of 5.9 μC, and V_{OC} of 0.63 V (Fig. 4g and Supplementary Figs. 36, 37), demonstrating stronger cooperative amplification of EDL-redox-photovoltaic coupling.

Beyond solid-state regulation, liquid-phase ionic composition provides an additional and effective tuning parameter. In the absence of triboelectric polarization and UV illumination, replacing water with concentrated electrolytes (1 M LiCl, HCl, and NaOH) significantly enhances the output to 0.72 mA, 0.86 mA, and 2.09 mA, respectively (Fig. 4h), accompanied by corresponding increases in Q_{SC} and V_{OC} (Supplementary Figs. 38, 39). This enhancement originates from the high ionic strength of the electrolytes, which reduces the Debye length, compresses the EDL, and accelerates ion migration within the dual-EDL system. Among the tested electrolytes, NaOH generates the highest performance due to its combined effects on interfacial wettability and reaction kinetics. The highly alkaline solution exhibits excellent wetting on p-Si (~12° contact angle; Fig. 4i), enabling the formation of dense EDLs and amplifying interfacial asymmetry. Meanwhile, p-Si undergoes non-passivating oxidation in NaOH, forming soluble silicates rather than a blocking oxide layer, thereby sustaining a continuous flux of reaction-derived ions that reinforces EDL enrichment (Fig. 4j). Under UV illumination, this system evolves into a photoactivated RC-IVNG, further boosting performance ($I_{SC} \approx 5.8$ mA, $Q_{SC} \approx 0.13$ mC, $V_{OC} \approx 0.76$ V; Fig. 4k and Supplementary Figs. 40, 41).

https://doi.org/10.1038/s41467-026-77245-1

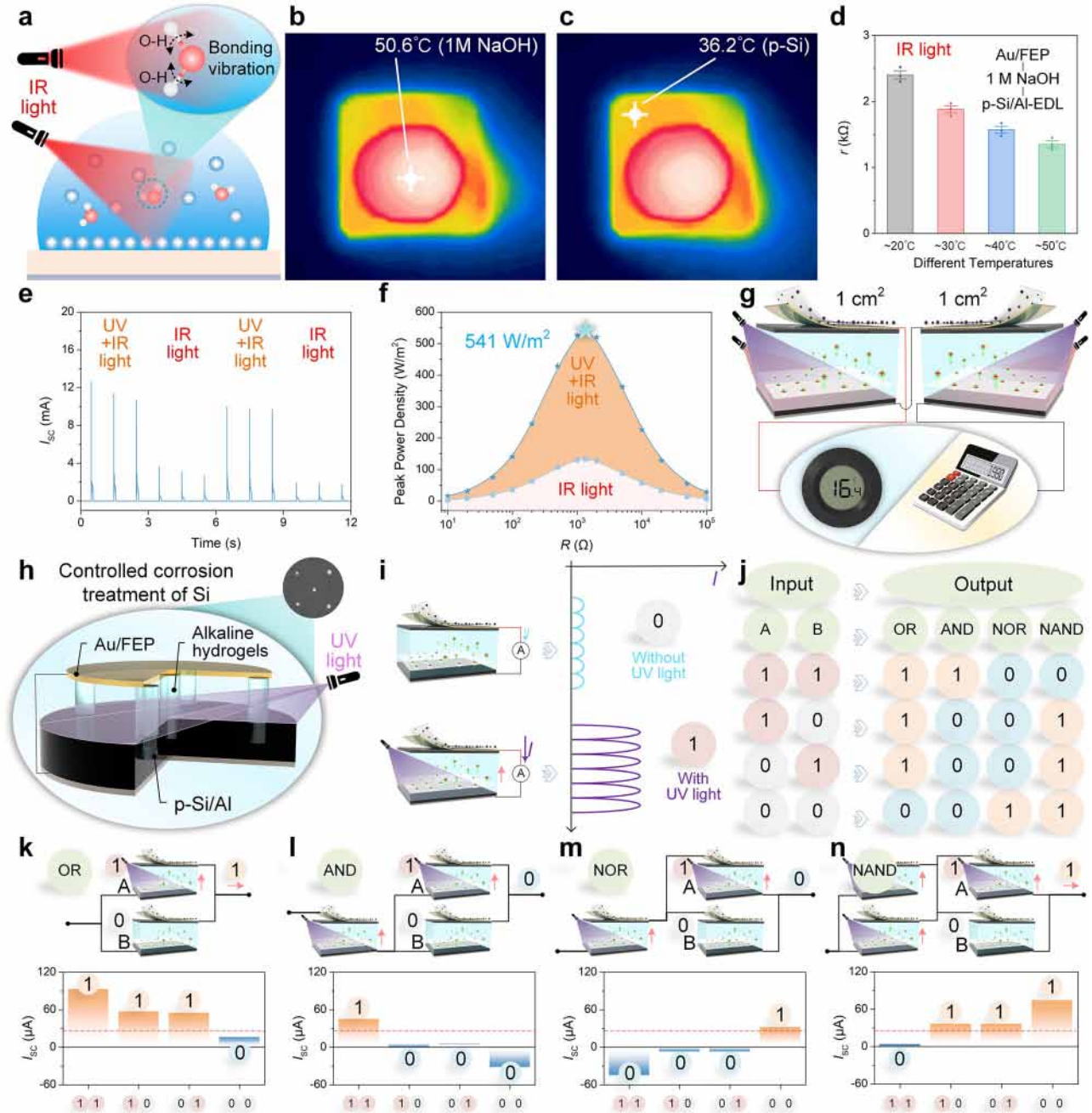


Fig. 5 | Output performance and multifunctionality of the RC-IVNG. a IR absorption of water via O-H overtone transitions enables efficient photothermal heating. **b**, **c** Selective IR-induced temperature rise in the electrolyte relative to the p-Si substrate, demonstrating preferential energy deposition in the liquid phase. **d** Decrease in internal resistance with increasing electrolyte temperature, indicating thermally enhanced ionic mobility. Error bars represent the standard deviation based on three replicate data. Source data are provided as a Source Data file. **e**, **f** Optimized device performance exhibiting a peak I_{SC} and P_R density of 541 W m^{-2}. **g** Two 1 cm^2 RC-IVNG units connected in series generate electrical output sufficient to drive low-power electronic devices, including a digital thermometer and calculator. The device output arises from triboelectrically induced ionic polarization and asymmetric EDLs, while the steady-state response is governed by coupled ionic transport and interfacial electrochemical processes. **h** Light-driven directional semiconductor etching enabled by photoactivated ionic flux in an alkaline hydrogel. **i** Distinct and stable ionic current states under different UV intensities, enabling optically addressable iontronic states. **j** Schematic of a light-gated iontronic logic architecture based on photonic modulation of interfacial ionic transport. **k**–**n** Demonstration of logic operations achieved solely through optical control of ionic migration.

Photogenerated holes drive interfacial oxidation along the same non-passivating pathway, generating additional ionic flux that cooperatively enhances the pre-existing EDL asymmetry. Collectively, these results establish three orthogonal control axes for iontrovoltaic systems: solid-state band engineering, interfacial energetic asymmetry, and liquid-phase ionic design. Their integration, together with optical or triboelectric stimuli, enables deterministic modulation of the ionic energy landscape and maximization of directional ion transport in the RC-IVNG.

Output performance and multi-directional applications of the RC-IVNG

To further accelerate ionic transport, photothermal activation was introduced by illuminating the 1 M NaOH electrolyte with IR radiation,

where water exhibits strong overtone absorption of O-H vibrations (Fig. 5a). This efficiently converts photon energy into heat, selectively raising the liquid temperature to ~50 °C while the p-Si substrate remains cooler with ~36 °C (Fig. 5b, c and Supplementary Figs. 42, 43). The resulting thermal activation reduces viscosity, enhances ionic diffusivity, and lowers the internal resistance of the RC-IVNG from ~2.4 kΩ to ~1.4 kΩ (Fig. 5d), thereby strengthening ionic transport within the asymmetric EDLs. When combined with triboelectric polarization and UV photoexcitation, this photothermal effect produces a pronounced cooperative amplification. Under these optimal conditions, the RC-IVNG delivers a V_{OC} of 0.9 V, I_{SC} of 12.6 mA, and Q_{SC} of 0.16 mC, corresponding to a P_R density of 541 W m^{-2} (Fig. 5e, f and Supplementary Figs. 44, 45), exceeding typical tribovoltaic nanogenerators[46–49], triboiontronic nanogenerators[50–52], and triboelectric nanogenerators[53–57] (Fig. 1e). As operation proceeds, progressive ionic redistribution and interfacial equilibration gradually reduce the asymmetry of EDLs, leading to a decay of the iontrovoltaic contribution. The system consequently evolves toward a quasi-steady state dominated by interfacial redox processes associated with Si oxidation and dissolution, generating a stable P_R density of ~311 W m^{-2} (Supplementary Fig. 46). Importantly, the difference between the initial peak output and the steady-state plateau provides a direct quantitative estimate of the intrinsic iontrovoltaic contribution, enabling its separation from the sustained Faradaic processes. These results indicate that the iontrovoltaic effect originates from interfacial ionic polarization and EDL asymmetry, whereas the steady-state output under strongly alkaline conditions is primarily governed by chemically driven electrochemical reactions involving electrode consumption. The enhanced output enables direct operation of low-power electronics. Two 1 cm^2 RC-IVNG units connected in series produce ~1.7 V (Supplementary Figs. 47, 48), sufficient to drive a digital thermometer and calculator (Fig. 5g, Supplementary Figs. 49, 50 and Supplementary Movie 1, 2). Operational stability tests show that I_{SC} output decreases from ~12.6 mA to ~1.8 mA over ~50 min due to electrolyte evaporation (Supplementary Fig. 51), but rapidly recovers to ~8.8 mA upon replenishment (Supplementary Fig. 52). Repeated cycling maintains stable output above ~7 mA, indicating good reversibility and durability. These results demonstrate that performance is primarily governed by reversible environmental factors, and can be further improved through encapsulation, microfluidic confinement, or continuous electrolyte supply.

Beyond efficient energy flow, the amplified ion flux was harnessed to actuate matter transformation. By inserting an alkaline hydrogel between the top Au/FEP and bottom p-Si/Al electrodes, UV illumination produced a flux of photogenerated holes that oxidized the semiconductor at the p-Si/hydrogel interface (Fig. 5h and Supplementary Fig. 53). In alkaline media, oxidation proceeded through silicate formation rather than SiO_2 passivation, enabling continuous, directional etching. Because hydrogels could be patterned arbitrarily, they define the spatial ionic microenvironment, rendering the etched geometry fully programmable by hydrogel shape and illumination pattern. This demonstrated that iontrovoltaics not only convert interfacial ionic motion into electrical energy but can also translate optical and electrochemical stimuli into deterministic, spatially resolved matter transformation, a direct manifestation of matter-energy coupling. Crucially, the same interfacial physics that govern energy harvesting could also endow the system with neuromorphic functionality. Owing to the strong coupling among photocarrier excitation, interfacial oxidation, and asymmetric EDL-mediated ion transport, the RC-IVNG displayed two well-resolved, reproducible steady-state current levels under different UV intensities (Fig. 5i). In darkness, the system stabilized at ~10 μA; under UV illumination, it transitioned to a high-current state of ~50 μA (Supplementary Fig. 54). These discrete plateaus provided a robust physical basis for optical encoding of iontronic states and parallel synaptic behavior, where presynaptic excitation modulates Ca^{2+} influx and neurotransmitter release to generate graded postsynaptic currents. Exploiting this behavior, a light-gated iontronic logic architecture was constructed. Two RC-IVNGs served as independently addressable input units A and B, with binary states assigned optically (0 = without UV; 1 = with UV) (Fig. 5j). Because each RC-IVNG intrinsically produced distinct steady-state ionic currents for these two illumination states, their outputs could be combined in series or parallel to implement Boolean logic. By defining current thresholds corresponding to logical 0 and 1, OR, AND, NOR, and NAND operations were executed solely through photonic control of interfacial ion transport (Fig. 5k–n and Supplementary Figs. 55–58). No transistors, external biases, or electronic logic elements were required, and computation emerged directly from ionic migration through optically sculpted interfacial energy landscapes. Together, these results establish iontrovoltaics as a physically embodied platform in which matter (ionic species), energy (electrostatic and photonic fields), and information (logic states) evolve coherently within the same interfacial framework. By unifying energy harvesting, matter modulation, and neuromorphic computation, the RC-IVNG transcended the conventional separation between power generation, sensing, and logic, offering a paradigm for matter-energy-information coupling in aqueous and soft environments.

Discussion

In summary, the iontrovoltaic effect was established as a previously unrecognized interfacial mechanism in which photogenerated charge separation, ionic transport, and electrochemical reactivity are intrinsically coupled at dynamically programmable semiconductor-liquid interfaces. By combining triboelectrically induced ion polarization with asymmetric EDL states, interfacial electrostatics can be actively reconfigured, simultaneously suppressing ionic screening, modulating the semiconductor SCR, and sustaining ion gradient potentials without chemical modification or external bias. Experimental evidence confirms this coupled regulation. Interfacial pH measurements reveal polarization-driven ionic redistribution within the EDL, while KPFM and Mott-Schottky analysis demonstrate reversible modulation of semiconductor band bending and SCR charge density. Together, these results establish the EDL as an active participant in charge separation rather than a passive screening layer. The resulting asymmetric EDLs generate spontaneous directional ionic transport, which is further amplified under illumination through efficient photocarrier separation and interfacial ion generation. This cooperative ionic-electronic coupling enables an RC-IVNG with a P_R density of 541 W m^{-2}, surpassing conventional triboelectric, tribovoltaic, and triboiontronic systems. Beyond energy conversion, dynamically programmable EDLs enable information encoding and processing through controlled ionic fluxes, supporting light-responsive iontronic gating and reconfigurable logic directly at the interface. In this framework, computation emerges from interfacial physicochemical dynamics rather than predefined electronic circuitry. More broadly, the iontrovoltaic effect defines a general principle for unifying energy conversion, matter transport, and information processing within a single interfacial system, providing a foundation for autonomous, low-power ionic-electronic architectures relevant to brain-inspired systems and embodied intelligence.

Methods

Materials

Single-crystal Si wafers were used as semiconductor substrates. Both p-type and n-type wafers had a thickness of 400 ± 25 μm, a (100) orientation, and a resistivity of 0.001-0.005 Ω·cm. The wafers were diced into 1 × 1 cm^2 chips and sequentially cleaned by ultrasonication in acetone, ethanol, and deionized water before use. For Au/FEP electrodes, a ~100 nm Au layer was deposited onto FEP films by magnetron sputtering (Discovery 635, Denton Vacuum, USA) at 50 W for 10 min with continuous rotation (40 rpm) to ensure uniform coverage.

For surface fluorination, Si wafers were first cleaned and hydroxylated in the solution (H_2SO_4/H_2O_2 = 7:3, v/v) for 1 h, followed by rinsing with deionized water and drying under nitrogen. FDTES (1H, 1H, 2H, 2H - Perfluorodecyltriethoxysilane) was dissolved in anhydrous isooctane (2.5–10 mmol L^{-1}), and the wafers were immersed for 12 h to obtain fluorinated Si (Si-F). The samples were then rinsed with isooctane and isopropanol and dried in air.

Device fabrication and operation

The IVNG and RC-IVNG were constructed in a vertical solid-liquid-solid configuration with an active area of 1 cm^2. For the bottom electrode, Au, Cu, or Al foils were attached to the backside of p-Si or n-Si substrates, while the front surface served as the semiconductor-liquid interface. Two types of top electrodes were employed. In the Si/Au configuration, metal layers were attached to the backside of the Si chip, leaving the front surface exposed to the electrolyte. In the Au/FEP configuration, a sputtered Au/FEP film served as the top electrode; nanoscale fissures in the thin Au layer allowed water penetration to the FEP surface, enabling rapid EDL formation. Triboelectric polarization was introduced by laminating an FEP layer onto the top electrode and rubbing it with electropositive fur for ~20 s, generating a stable negative surface potential. The applied contact force during operation was ~35–40 N, measured using a calibrated pressure sensor (ZMF-500, Hemuele, China), under which stable and reproducible triboelectric polarization was achieved. For operation, ~300 µL of water or electrolyte was dispensed onto the bottom Si surface. The top electrode was actuated using a linear motor to precisely control approach and separation, enabling programmed sequential wetting and the formation of asymmetric EDLs. All experiments were conducted under ambient conditions.

Optical excitation

UV illumination (365 nm) was provided by a commercial LED source (LedHand12, Holisin, China). At a distance of ~25 mm, the illumination area was ~10 mm in diameter with a nominal power density of ~1800 mW cm^{-2}. IR irradiation was supplied by a broadband infrared lamp (IR lamp, Kelishi, China); at ~100 mm distance, the spot diameter was ~200 mm with a nominal power density of ~790 mW cm^{-2}.

Electrical characterization

Electrical outputs of the IVNG and RC-IVNG were measured under controlled mechanical actuation using a linear motor (PL0119 × 600/520, LinMot, Switzerland), enabling precise regulation of electrode approach-separation dynamics. Current and charge signals were recorded with a higher-impedance electrometer (6514, Keithley, USA), while voltage signals were acquired using a data acquisition system (BNC−2120, National Instruments, USA). All measurements were conducted under ambient conditions without external electrical bias.

Statistics & reproducibility

No statistical method was used to predetermine sample size. No data were excluded from the analyses. The experiments were not randomized. The investigators were not blinded to allocation during experiments and outcome assessment. All experiments were independently repeated to ensure reproducibility.

Electrochemical measurement

Electrochemical (Mott-Schottky) measurements were performed using a three-electrode configuration. The working electrode consisted of a 1 cm × 1 cm silicon substrate with a copper back contact for charge extraction. A gallium-indium-tin (GaInSn) alloy was applied between the silicon and copper interface to improve electrical contact, and the device was encapsulated using hot-melt adhesive to prevent electrolyte exposure except at the active sensing surface. Platinum foil (0.5 cm × 0.5 cm, thickness 1 mm) was used as the counter electrode, and Ag/AgCl served as the reference electrode. The electrolyte was deionized water. For electrochemical testing, the potential window was set to 0.5-1 V around the open-circuit voltage, with the initial and final potentials defined symmetrically. The amplitude was 0.01 V, and the frequency was maintained at 1000.

Reporting summary

Further information on research design is available in the Nature Portfolio Reporting Summary linked to this article.

Data availability

The data supporting the findings of this study are reported in the main text or the Supplementary Information. All raw experimental data relevant to this study are available from the corresponding author upon request. Source data are provided in this paper.

References

1. LaPotin, A. et al. Thermophotovoltaic efficiency of 40%. *Nature* **604**, 287–291 (2022).
2. Xing, F. et al. High-Entropy Energy for Self-Powered Systems. *SmartSys* **1**, e70001 (2025).
3. Unalan, H. E. et al. ZnO Nanowire and WS_2 Nanotube Electronics. *IEEE T. Electron Dev.* **55**, 2988–3000 (2008).
4. Wei, D. Writable electrochemical energy source based on graphene oxide. *Sci. Rep.* **5**, 15173 (2015).
5. Canil, L. et al. Tuning halide perovskite energy levels. *Energy Environ. Sci.* **14**, 1429–1438 (2021).
6. Zhang, C. et al. Ti1–graphene single-atom material for improved energy level alignment in perovskite solar cells. *Nat. Energy* **6**, 1154–1163 (2021).
7. Song, K. et al. Toward efficient utilization of photogenerated charge carriers in photoelectrochemical systems: engineering strategies from the atomic level to configuration. *Chem. Rev.* **124**, 13660–13680 (2024).
8. Wang, H., Tian, Y.-M. & Konig, B. Energy- and atom-efficient chemical synthesis with endergonic photocatalysis. *Nat. Rev. Chem.* **6**, 745–755 (2022).
9. Wu, X., Van Waeyenberg, J., Vangestel, D. & Sels, B. The overlooked solvent effects: a reconsideration of the paradigm in semiconductor photocatalysis. *Energy Environ. Sci.* **18**, 1191–1204 (2025).
10. Laskowski, F. A. L. et al. Nanoscale semiconductor/catalyst interfaces in photoelectrochemistry. *Nat. Mater.* **19**, 69–76 (2020).
11. Du, D. et al. Photoelectrochemistry of oxygen in rechargeable Li-O_2 batteries. *Chem. Soc. Rev.* **51**, 1846–1860 (2022).
12. Deka Boruah, B. et al. Vanadium dioxide cathodes for high-rate photo-rechargeable zinc-ion batteries. *Adv. Energy Mater.* **11**, 2100115 (2021).
13. Wen, Z. et al. Engineered band alignment of semiconductive nanofluidics for photo-electro-ion mediated ultrahigh osmotic energy harvesting. *Adv. Funct. Mater.* **35**, 2425595 (2025).
14. Zheng, L., Zhu, X. & Xiao, K. Photo-iontronics: mechanisms and manipulation for neuromorphic vision. *Iontronics* **2**, 10 (2026).
15. Chen, X. et al. Engineering facet-dependent interface charge transfer in liquid metal-embraced BiVO4 photoelectrodes for efficient photoelectrochemical water splitting. *Adv. Funct. Mater.* **34**, 2409566 (2024).
16. Holtus, T. et al. Shape-preserving transformation of carbonate minerals into lead halide perovskite semiconductors based on ion exchange/insertion reactions. *Nat. Chem.* **10**, 740–745 (2018).
17. Liu, Z. et al. Contact-electro-catalysis at dynamic semiconductor-water junctions. *Research* **8**, 0940 (2025).
18. Dong, H. et al. Potential window alignment regulating ion transfer in faradaic junctions for efficient photoelectrocatalysis. *Nat. Commun.* **14**, 7969 (2023).

19. Shi, J. et al. Eliminating the electric field response in a perovskite heterojunction solar cell to improve operational stability. *Sci. Bull.* **66**, 536–544 (2021).
20. Gudjonsdottir, S. & Houtepen, A. J. Permanent electrochemical doping of quantum dots and semiconductor polymers. *Adv. Funct. Mater.* **30**, 2004789 (2020).
21. Wang, Y. et al. Unveiling catalytic sites in a typical hydrogen photogeneration system consisting of semiconductor quantum dots and 3d-metal ions. *J. Am. Chem. Soc.* **142**, 4680–4689 (2020).
22. Benetti, D. & Rosei, F. A bridge for charge carriers. *Nat. Energy* **4**, 910–911 (2019).
23. Zhou, Y., Zhao, H., Ma, D. & Rosei, F. Harnessing the properties of colloidal quantum dots in luminescent solar concentrators. *Chem. Soc. Rev.* **47**, 5866–5890 (2018).
24. Xiang, L. et al. Nanoscale doping of polymeric semiconductors with confined electrochemical ion implantation. *Nat. Nanotechnol.* **19**, 1122–1129 (2024).
25. Ishii, M. et al. Doping of molecular semiconductors through proton-coupled electron transfer. *Nature* **622**, 285–291 (2023).
26. Xiang, L. et al. Ion-gating engineering of organic semiconductors toward multifunctional devices. *Adv. Funct. Mater.* **31**, 2102149 (2021).
27. de Rojas, J. et al. Boosting room-temperature magneto-ionics in a non-magnetic oxide semiconductor. *Adv. Funct. Mater.* **30**, 2003704 (2020).
28. Long, Y. et al. Smart hydrogel tactile sensors and systems: a comprehensive review. *SmartSys* **1**, e70015 (2026).
29. Wei, Y. et al. Probing electrical double layer via triboelectric charge transfer. *Nat. Commun.* **17**, 402 (2026).
30. Zhuang, P. et al. Solid-liquid interface lubricating hydrogels for tendon-bone healing. *Research* **8**, 0924 (2025).
31. Luo, C. et al. CNT array-based aluminum bipolar electrode iontronic memristors. *Iontronics* **2**, 6 (2026).
32. Lin, S., Chen, X. & Wang, Z. L. The tribovoltaic effect and electron transfer at a liquid-semiconductor interface. *Nano Energy* **76**, 105070 (2020).
33. Lin, S., Chen, X. & Wang, Z. L. Contact electrification at the liquid-solid interface. *Chem. Rev.* **122**, 5209–5232 (2022).
34. Luo, N., Duan, W., Yakobson, B. I. & Zou, X. Excitons and electron–hole liquid state in 2D γ-phase group-IV monochalcogenides. *Adv. Funct. Mater.* **30**, 2000533 (2020).
35. Pham, T. A., Lee, D., Schwegler, E. & Galli, G. Interfacial effects on the band edges of functionalized si surfaces in liquid water. *J. Am. Chem. Soc.* **136**, 17071–17077 (2014).
36. Sun, L. et al. Efficient electrical doping of organic semiconductors via an orthogonal liquid-liquidcontact. *Adv. Funct. Mater.* **31**, 2009660 (2021).
37. Chen, Y. et al. Dynamic coupling of photoinduced charges with evaporation-driven unipolar ion flow in semiconducting nanochannels. *Small* **21**, e11802 (2025).
38. Wang, X., Ivanov, A. P. & Edel, J. B. Biocompatible biphasic iontronics enable neuron-like ionic signal transmission. *Research* **7**, 0294 (2024).
39. Willatzen, M. & Wang, Z. L. Contact electrification by quantum-mechanical tunneling. *Research* **2019**, 6528689 (2019).
40. Wei, Y. et al. Contact electrification at the solid-liquid transition interface. *Mater. Today* **74**, 2–11 (2024).
41. Li, R. et al. Probing Leidenfrost effect via contact electrification. *Nano Energy* **134**, 110570 (2025).
42. Li, X., Wang, Z. L. & Wei, D. Scavenging energy and information through dynamically regulating the electrical double layer. *Adv. Funct. Mater.* **34**, 2405520 (2024).
43. Li, X., Cheng, T., Wang, Z. L. & Wei, D. Neuromimetic circuits enabled by dynamic regulation of the electrical double layer. *Npj Flex. Electron.* **9**, 66 (2025).
44. Wang, Z. L. & Wang, A. C. On the origin of contact-electrification. *Mater. Today* **30**, 34–51 (2019).
45. Lin, S., Xu, L., Wang, A. C. & Wang, Z. L. Quantifying electron-transfer in liquid-solid contact electrification and the formation of electric double-layer. *Nat. Commun.* **11**, 399 (2020).
46. Meng, J. et al. Durable flexible direct current generation through the tribovoltaic effect in contact-separation mode. *Energy Environ. Sci.* **15**, 5159–5167 (2022).
47. Zhang, Z. et al. Semiconductor contact-electrification-dominated tribovoltaic effect for ultrahigh power generation. *Adv. Mater.* **34**, e2200146 (2022).
48. Liu, J. et al. Separation and quantum tunneling of photo-generated carriers using a tribo-Induced field. *Matter* **1**, 650–660 (2019).
49. Deng, S., Seh, W. & Zhang, Q. Thermal characteristics of tribovoltaic dynamic Schottky junctions. *Nano Energy* **114**, 108665 (2023).
50. Li, X. et al. Triboiontronics with temporal control of electrical double layer formation. *Nat. Commun.* **15**, 6182 (2024).
51. Li, X. et al. Triboiontronics for efficient energy and information flow. *Matter* **6**, 3912–3926 (2023).
52. Li, X. et al. Harnessing triboiontronic Maxwell's demon by triboelectric-induced polarization for efficient energy-information flow. *Joule* **9**, 101888 (2025).
53. Xu, W. et al. A droplet-based electricity generator with high instantaneous power density. *Nature* **578**, 392–396 (2020).
54. Dong, Y. et al. Gas-liquid two-phase flow-based triboelectric nanogenerator with ultrahigh output power. *Sci. Adv.* **8**, eadd0464 (2022).
55. Wu, P. et al. Boosting the output of liquid–solid triboelectric nanogenerator by an external charge-pumping strategy. *Adv. Energy Mater.* **14**, 2303912 (2024).
56. Cao, V. A. et al. Output power density enhancement of triboelectric nanogenerators via ferroelectric polymer composite interfacial layers. *Nano Energy* **67**, 104300 (2020).
57. Kim, M. et al. Remarkable output power density enhancement of triboelectric nanogenerators via polarized ferroelectric polymers and bulk MoS_2 composites. *ACS Nano* **13**, 4640–4646 (2019).
58. Zhang, Z. et al. An ultrahigh power density and ultralow wear GaN-based tribovoltaic nanogenerator for sliding ball bearing as self-powered wireless sensor node. *Adv. Mater.* **36**, e2310098 (2024).
59. Fu, Y. & Ruan, H. Advanced modular rotary triboelectric nanogenerator: Pushing boundaries in peak power density and impedance reduction. *Nano Energy* **134**, 110557 (2025).

Author contributions

D.W. and Z.L.W. proposed the idea and the project. D.W. designed all the experiments and supervised the whole project. Y.C. carried out the Mott-Schottky measurements and assisted in reviewing and revising the manuscript. X.L. carried out the main experiments in this paper and analyzed the corresponding data. Yu Wei conducted application experiments related to energy flow. Y.O. developed a light-driven iontronic logic control method. All the authors discussed the results and commented on the manuscript. D.W. and X.L. wrote this paper.

Funding

This work was supported by China Postdoctoral Science Foundation (certificate number 2025M781041) and National Natural Science Foundation (grant number 22479016).

Competing interests

The authors declare no competing interests.

Additional information

Supplementary information The online version contains supplementary material available at https://doi.org/10.1038/s41467-026-77245-1.

Correspondence and requests for materials should be addressed to Yuying Cao or Di Wei.

Peer review information *Nature Communications* thanks Jérémy Odent and the other anonymous reviewer for their contribution to the peer review of this work. A peer review file is available.

Reprints and permissions information is available at http://www.nature.com/reprints

Publisher's note Springer Nature remains neutral with regard to jurisdictional claims in published maps and institutional affiliations.

Open Access This article is licensed under a Creative Commons Attribution-NonCommercial-NoDerivatives 4.0 International License, which permits any non-commercial use, sharing, distribution and reproduction in any medium or format, as long as you give appropriate credit to the original author(s) and the source, provide a link to the Creative Commons licence, and indicate if you modified the licensed material. You do not have permission under this licence to share adapted material derived from this article or parts of it. The images or other third party material in this article are included in the article's Creative Commons licence, unless indicated otherwise in a credit line to the material. If material is not included in the article's Creative Commons licence and your intended use is not permitted by statutory regulation or exceeds the permitted use, you will need to obtain permission directly from the copyright holder. To view a copy of this licence, visit http://creativecommons.org/licenses/by-nc-nd/4.0/.

© The Author(s) 2026